2015

Low trap-state density and long carrier diffusion in organolead trihalide perovskite single crystals

Dong Shi
King Abdullah University of Science and Technology (KAUST)

Valerio Adinolfi
University of Toronto

Riccardo Comin
University of Toronto

Mingjian Yuan
University of Toronto

Erkki Alarousu
King Abdullah University of Science and Technology (KAUST)

See next page for additional authors

Published 30 January 2015 in *Science* **347**, 519 (2015); doi: 10.1126/science.aaa2725

Low trap-state density and long carrier diffusion in organolead trihalide perovskite single crystals

Dong Shi,[1]* Valerio Adinolfi,[2]* Riccardo Comin,[2] Mingjian Yuan,[2] Erkki Alarousu,[1] Andrei Buin,[2] Yin Chen,[1] Sjoerd Hoogland,[2] Alexander Rothenberger,[1] Khabiboulakh Katsiev,[1] Yaroslav Losovyj,[3] Xin Zhang,[4] Peter A. Dowben,[4] Omar F. Mohammed,[1] Edward H. Sargent,[2] and Osman M. Bakr[1]

1 Solar and Photovoltaic Engineering Research Center (SPERC), King Abdullah University of Science and Technology (KAUST), 23955-6900 Thuwal, Saudi Arabia
2 Department of Electrical and Computer Engineering, University of Toronto, Toronto, Ontario M5S 3G4, Canada
3 Department of Chemistry, Indiana University, Bloomington, IN 47405, USA
4 Department of Physics and Astronomy, University of Nebraska–Lincoln, Lincoln, NE 68588, USA
* These authors contributed equally to this work.
Corresponding author — O.M. Bakr, email osman.bakr@kaust.edu.sa

Abstract
The fundamental properties and ultimate performance limits of organolead trihalide $MAPbX_3$ ($MA = CH_3NH_3^+$; $X = Br^-$ or I^-) perovskites remain obscured by extensive disorder in polycrystalline $MAPbX_3$ films. We report an antisolvent vapor-assisted crystallization approach that enables us to create sizable crack-free $MAPbX_3$ single crystals with volumes exceeding 100 cubic millimeters. These large single crystals enabled a detailed characterization of their optical and charge transport characteristics.We observed exceptionally low trap-state densities on the order of 10^9 to 10^{10} per cubic centimeter in $MAPbX_3$ single crystals (comparable to the best photovoltaic-quality silicon) and charge carrier diffusion lengths exceeding 10 micrometers. These results were validated with density functional theory calculations.

Solution-processed hybrid organolead trihalide ($MAPbX_3$) perovskite solar cells (PSCs) have now achieved 20.1% certified power conversion efficiencies (1), following a rapid surge of development since perovskite based devices were first reported in 2009 (2). A key to the success of PSCs is the long diffusion length of charge carriers in the absorber perovskite layer (3). This parameter is expected to depend strongly on film crystallinity and morphology. Thermally evaporated $MAPbI_3$ films fabricated using a Cl^--based metal salt precursor were reported to exhibit carrier diffusion lengths three times those of the best solution-processed materials, yet no measurable Cl^- was incorporated in the final films, hinting at amajor but unclear mechanism in the control of crystallinity and morphology (4, 5). These observations suggest that there may be room to improve upon already remarkable PSC efficiencies via the optimization of three key parameters: charge carrier lifetime, mobility, and diffusion length.

The quest for further improvements in these three figures of merit motivated our exploration of experimental strategies for the synthesis of large single-crystal $MAPbX_3$ perovskites that would exhibit phase purity and macroscopic (millimeter) dimensions. Unfortunately, previously published methods failed to produce single crystals with macroscopic dimensions large enough to enable electrode deposition and practical characterization of electrical properties (6). Past efforts based on cooling-induced crystallizationwere hindered by (i) the limited extent to which solubility could be influenced by controlling temperature, (ii) the complications arising from temperature-dependent phase transitions inMAPbX3, and(iii) the impact of convective currents (arising from thermal gradients in the growth solution) that disturb the ordered growth of the crystals.

We hypothesized that a strategy using antisolvent vapor-assisted crystallization (AVC), in which an appropriate antisolvent is slowly diffused into a solution containing the crystal precursors, could lead to the growth of sizableMAPbX3 crystals of high quality (with crack-free, smooth surfaces,well-shaped borders, and clear bulk transparency). Prior attempts to grow hybrid perovskite crystals with AVC have fallen short of these qualities—a fact we tentatively attributed to the use of alcohols as antisolvents (7). Alcohols act as good solvents for the organic salt MAX (8) due to solvent-solute hydrogen bond interactions; as a result, they can solvate MA+ during the ionic assembly of the crystal, potentially disrupting long-range lattice order.

We instead implemented AVC (Fig. 1A) using a solvent with high solubility and moderate coordination for MAX and PbX_2 [N,Ndimethylformamide (DMF) or g-butyrolactone (GBA)] and an antisolvent in which both perovskite precursors are completely insoluble [dichloromethane (DCM)]. We reasoned that DCM, unlike alcohols, is an extremely poor solvent for both MAX and PbX_2 and lacks the ability to form hydrogen bonds, thus minimizing asymmetric interactions with the ions during their assembly into crystal form. When combined with a slow and controlled diffusion rate into DMF or GBA, our approach established the conditions for all the ionic building blocks of the perovskite to be coprecipitated from solution stoichiometrically. Using this method, we grew high-quality, millimeter-sized $MAPbBr_3$ and MAPbI3 single crystals (fig. S1) (9) whose shape conformed to the underlying symmetry of the crystal lattice. The phase purity of the as-grown crystals was confirmed by x-ray diffraction (XRD) performed on powder ground from a large batch of crystals (Fig. 1B).

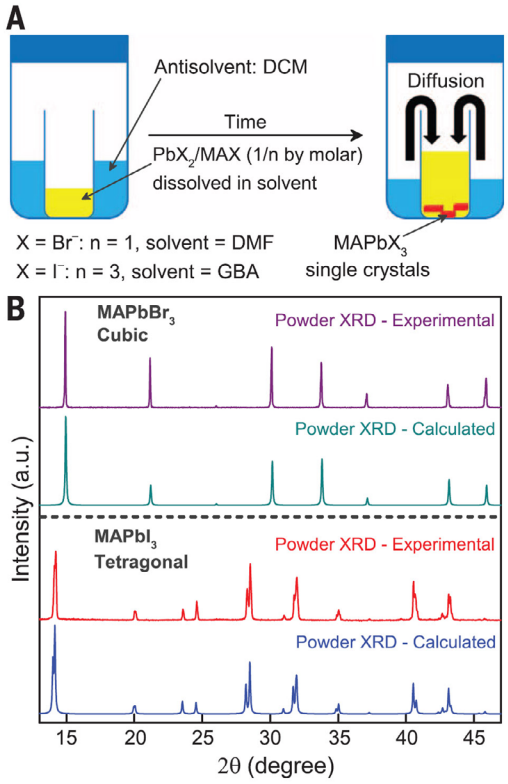

Fig. 1. Crystal growth and diffraction. (A) Schematic diagram of the crystallization process. (B) Experimental and calculated powder XRD profiles confirming the phase purity of $MAPbX_3$ crystals grown at room temperature (fig. S1). Single-crystal XRD data are given in (9).

The synthesized crystals were of sufficient quality and macroscopic dimensions to enable a detailed investigation of the optical and charge transport properties. The absorbance of$MAPbX_3$ (X = Br– or I–) (Fig. 2) shows a clear band edge cutoff with no excitonic signature, which suggests a minimal number of in-gap defect states. For comparison, the absorption spectrum from the polycrystalline $MAPbBr_3$ (fig. S2) (9) and $MAPbI_3$ (5) thin films shows a peak near the band gap, which is often attributed to an excitonic transition. This observation is consistent with a substantial amount of disorder and lack of long-range structural coherence in nanostructured thin films (10). By extrapolating the linear region of the absorption edge to the energy-axis intercept (fig. S3) (9), we determined the optical band gaps of $MAPbBr_3$ and $MAPbI_3$ single crystals to be 2.21 and 1.51 eV (Fig. 2), respectively. Both materials in their single-crystalline form exhibit a substantially narrower band gap than the corresponding films, which could enhance photon harvesting and hence improve photocurrent generation.

As also shown in Fig. 2, both $MAPbBr_3$ and $MAPbI_3$ exhibit a narrow photoluminescence (PL) that peaks near the band edge. A noticeable shoulder at ~790 nm in the PL of $MAPbI_3$ single crystals is in agreement with the PL from thin films (5), with the main PL peaking at 820 nm attributed to the intrinsic PL from the $MAPbI_3$ crystal lattice. A more structured PL spectrum was observed for polycrystalline $MAPbBr_3$ thin films (fig. S2) (9).

We investigated the key quantities that directly affect a material's potential for application in PSCs: carrier lifetime t, carrier mobility m, and carrier diffusion length LD. In addition, we estimated the in-gap trap density ntraps in order to correlate the trap density with the observed diffusion length. For$MAPbBr_3$ single crystals, we firstmeasured carrier mobility using the time-offlight technique (11). The transient current was measured for various driving voltages (V), and the corresponding traces are shown in Fig. 3A on a bilogarithmic scale. The transit time tt, defined as the position of the kink in the time traces, is marked by the blue squares, and the corresponding values are plotted in Fig. 3B as a function of V^{-1}. The mobility m [$m = mp \approx mn$, where mp and mn are the hole and electron mobility, respectively (12, 13)] can be directly estimated from the transit time tt, sample thickness d, and applied voltage V as $m = d^2/Vt_t$ (Fig. 3B) (9). Estimating mobility via a linear fit of tt versus V^{-1} led to an estimate of 115 $cm^2\ V^{-1}\ s^{-1}$. Complementary Hall effect measurements at room temperature confirmed a carrier (holes) concentration of between 5×10^9 and 5×10^{10} cm^{-3}, and provided amobility estimate in the range from 20 to 60 $cm^2\ V^{-1}\ s^{-1}$. Slightly lower mobilities obtained via the Hall effect may be ascribed to surface effects that are negligible for time-of-flight, which constitutes a bulk probe.

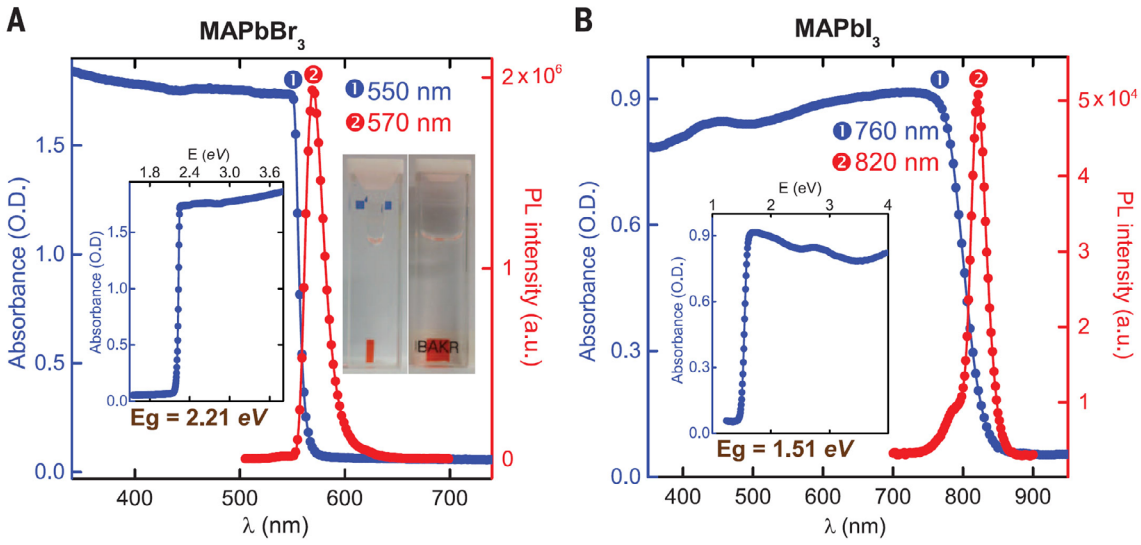

Fig. 2. Steady-state absorbance and photoluminescence. (A) $MAPbBr_3$ single crystal. (B) $MAPbI_3$ single crystal. Insets: Absorbance versus photon energy and the determined band gap Eg. PL excitation wavelength was 480 nm.

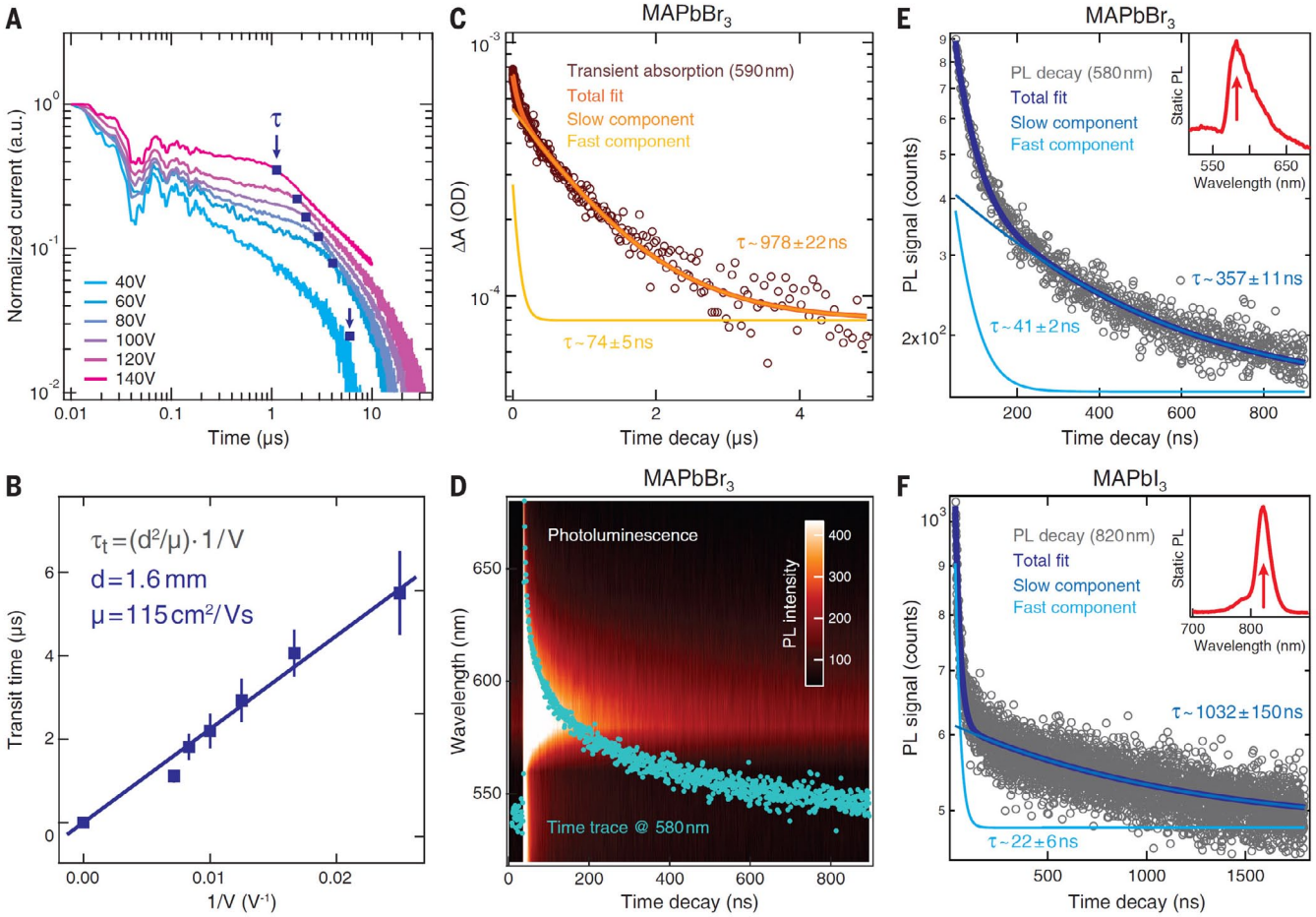

Fig. 3. Carrier mobility and lifetime measurements. (A) Time-of-flight traces showing the transient current after photoexcitation at time t = 0 in a bi-logarithmic plot; the transit time t_t is identified by the corner in each trace and marked by blue squares. (B) Linear fit of transit time versus inverse voltage V^{-1}. (C) Transient absorption in $MAPbBr_3$ crystals, evaluated at 590 nm, showing a fast component (t ± 74 T 5 ns) together with a slower decay (t ± 978 T 22 ns). (D) Time- and wavelength-dependent photoluminescence (PL) color map, with the time trace at l = 580 nm superimposed (blue markers). (E) PL time decay trace on a MAPbBr3 crystal at l = 580 nm,with biexponential fits showing a fast (t ± 41 T 2 ns) and a slowtransient (t ± 357 T 11 ns). (F) PL time decay trace on a MAPbI3 crystal (l = 820 nm, also showing a fast (t ± 22 T 6 ns) and a slow (t ± 1032 T 150 ns) component.

For $MAPbI_3$ single crystals, we estimated the carrier mobility using the space-charge-limited current (SCLC) technique. We measured the current-voltage (I-V) trace for the crystals and observed a region showing a clear quadratic dependency of the current on the applied voltage at 300 K (see fig. S8 for details). From this region, we could conservatively estimate the carrier mobility, obtaining the value m = 2.5 $cm^2\ V^{-1}\ s^{-1}$. Fromthe linear ohmic region, we also identified the conductivity of the crystal to be s = 1×10^{-8} $(ohm{\cdot}cm)^{-1}$. Combining the information on mobility and conductivity, we estimated a carrier concentration of nc = s/em ≈ 2×10^{10} cm^{-3} (where e is the electronic charge).

We estimated the carrier lifetime t from transient absorption (TA) and PL spectra. Nanosecond pump-probe TA spectroscopy was carried out over a window covering the nanosecond-tomicrosecond time scales in order to evaluate the fast (t ≈ 74 ns) as well as the slow (t ≈ 978 ns) carrier dynamics, as determined from bi-exponential fits. Time (t)– and wavelength (l)–resolved PL maps IPP(t, l) (Fig. 3D) of single-crystalline $MAPbBr_3$ were acquired in the wavelength region around the main band-to-band recombination peak at 580 nm (l = 500 to 680 nm). The time-dependent PL signals in single-crystalline samples of $MAPbBr_3$ and $MAPbI_3$ are shown in Fig. 3, E and F, respectively; the data were measured at the wavelength of themain PL peak—i.e., l = 580 nm and l = 820 nm for $MAPbBr_3$ and $MAPbI_3$, respectively (see insets).

The time-resolved traces are representative of the transient evolution of the electron-hole population after impulsive (Dt ≈ 0.7 ns) photoexcitation. Biexponential fits were performed to quantify the carrier dynamics (fig. S4, blue traces) (9). Both the bromide- and iodide-based perovskite crystals exhibited a superposition of fast and slow dynamics: t ≈ 41 and 357 ns for $MAPbBr_3$, and t ≈ 22 and 1032 ns for $MAPbI_3$. We assign these two very different time scales to the presence of a surface component (fast) together with a bulk component (slow), which reveals the lifetime of carriers propagating deeper in the material. The relative contribution of these two terms to the static PL can be readily evaluated by integrating the respective exponential traces (the integral is equal to the product of the amplitude A and the decay time t), which shows that the fast (tentatively surface) component amounts to only 3.6% of the total TA signal in $MAPbBr_3$, and to 12% and 7% of the total PL signal in $MAPbBr_3$ and $MAPbI_3$, respectively. Ultimately, by combining the longer (bulk) carrier lifetimes with the higher measured bulk mobility, we obtained a best-case carrier diffusion length LD=($k_BT/e \cdot \mu$

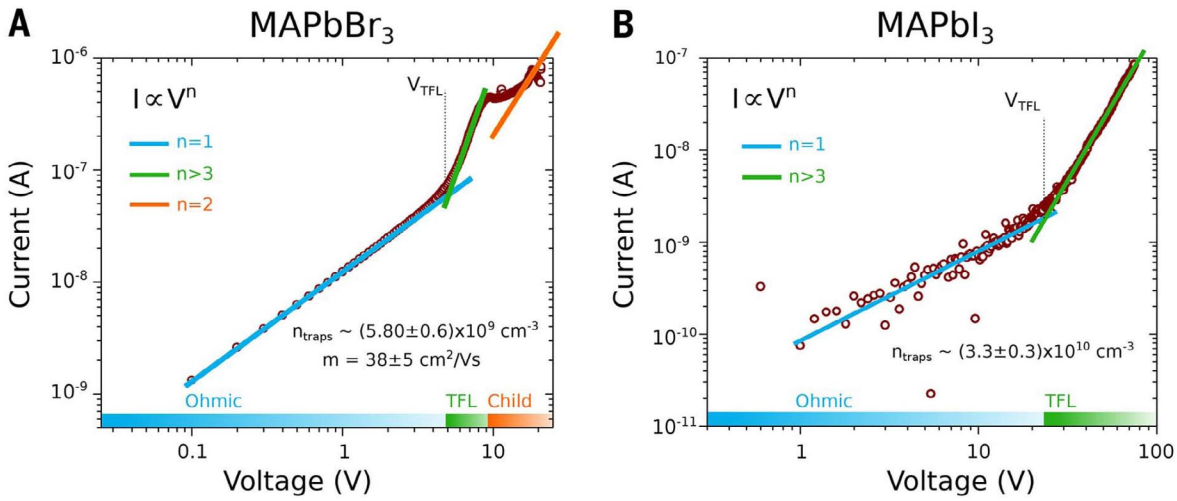

Fig. 4. Current-voltage traces and trap density. Characteristic I-V trace (purple markers) showing three different regimes for (A)$MAPbBr_3$ (at 300 K) and (B)$MAPbI_3$ (at 225 K). A linear ohmic regime (I ∞ V, blue line) is followed by the trap-filled regime, marked by a steep increase in current (I V $V^{n>3}$, greenline).The $MAPbBr_3$ trace shows a trap-free Child's regime (I ∞ V^2, green line) at high voltages.

·t)$^{1/2}$ (where kB is Boltzmann's constant and T is the sample temperature) of ~17 mm in$MAPbBr_3$; use of the shorter lifetime and lower mobility led to an estimate of ~3 mm. The same considerations were applied for the MAPbI3 crystals to obtain a best-case diffusion length of ~8 mm and a worst-case length of ~2 mm. For comparison, we also investigated the PL decay of solution-processed thin films of MAPbBr3 (fig. S5). We again found two dynamics: a fast decay (t ≈ 13 ns) and a longer-lived component (t ≈ 168 ns), in both cases faster than the single crystals. This result suggests a larger trap-induced recombination rate in the thin films, which are expected to possess a much higher trap density than the single crystals. Previous studies on non–Cl-doped $MAPbI_3$ nanostructured thin films also corroborate this trend, revealing a PL lifetime of ~10 ns and a carrier diffusion length of ~100 nm (3, 5).

Crystalline$MAPbX_3$ is characterized by a charge transport efficiency that outperforms thin film– based materials in mobility, lifetime, and diffusion length. To unveil the physical origins of this difference, we investigated the concentration of in-gap deep electronic trap states. We measured the I-V response of the crystals in the SCLC regime (Fig. 4). Three regions were evident in the experimental data. At low voltages, the I-V response was ohmic (i.e., linear), as confirmed by the fit to an I ≈ V functional dependence (blue line). At intermediate voltages, the current exhibited a rapid nonlinear rise (set in at VTFL = 4.6 V for $MAPbBr_3$ and 24.2 V for $MAPbI_3$) and signaled the transition onto the trap-filled limit (TFL)—a regime in which all the available trap states were filled by the injected carriers (14). The onset voltage VTFL is linearly proportional to the density of trap states ntraps (Fig. 4A). Correspondingly, we found for $MAPbBr_3$ single crystals a remarkably low trap density ntraps = 5.8×10^9 cm^{-3}, which, togetherwith the extremely clean absorption and PL profiles (see again Fig. 2A), points to a nearly defect-free electronic structure. At high fields, the current showed a quadratic voltage dependence in the Child's regime. In this region, we extracted the value for the trapfree mobility m. We found m = 38 cm^2 V^{-1} s^{-1} (Fig. 4A), a value in good agreement with the mobility extracted using time-of-flight and Hall effect measurements (fig. S7) (9). We determined a comparable low trap density ntraps = 3.3×10^{10} cm^{-3} for MAPbI3 single crystals using the same method (Fig. 4B).

The defect density measured for the room temperature–grown MAPbX3 crystals was superior to a wide array of established and emerging optoelectronic inorganic semiconductors including polycrystalline Si (ntraps ≈ 1013 to 1014 cm–3) (15, 16), CdTe/CdS (ntraps ≈ 10^{11} to 10^{13} cm^{-3}) (17), and copper indiumgalliumselenide (CIGS) (ntraps ≈ 10^{13} cm–3) thin films (18), as well as organic materials such as single-crystal rubrene (ntraps≈1016cm–3) (19) and pentacene (ntraps ≈ 10^{14} to 10^{15} cm–3) (20). Only ultra high-quality crystalline silicon, grown at high temperatures, offers comparable or better deep trap densities (108 < ntraps < 1015 cm–3) (21, 22). The exceptionally low trap density found experimentally can be explained with the aid of density functional theory (DFT) calculations performed on MAPbBr3,which predict a high formation energy for deep trap defects when $MAPbBr_3$ is synthesized under Br-rich conditions (e.g., from $PbBr_2$ and MABr), such as is the case in this study (9).

Acknowledgments — We thank N. Kherani, B. Ramautarsingh, A. Flood, and P. O'Brien for the use of the Hall setup. Supported by KAUST (O.M.B.) and by KAUST award KUS-11-009-21, the Ontario Research Fund Research Excellence Program, and the Natural Sciences and Engineering Research Council of Canada (E.H.S.).

REFERENCES AND NOTES

1. National Renewable Energy Laboratory, Best Research-Cell Efficiencies; www.nrel.gov/ncpv/images/efficiency_chart.jpg.
2. A. Kojima, K. Teshima, Y. Shirai, T. Miyasaka, J. Am. Chem. Soc. 131, 6050–6051 (2009).
3. T. C. Sum, N. Mathews, Energy Environ. Sci. 7, 2518–2534 (2014).
4. C. Wehrenfennig, M. Liu, H. J. Snaith, M. B. Johnston, L. M. Herz, Energy Environ. Sci. 7, 2269–2275 (2014).

5. S. D. Stranks et al., Science 342, 341–344 (2013).
6. D. B. Mitzi, Prog. Inorg. Chem. 48, 1–121 (1999).
7. Y. Tidhar et al., J. Am. Chem. Soc. 136, 13249–13256 (2014).
8. M. Xiao et al., Angew. Chem. Int. Ed. 53, 9898–9903 (2014).
9. See supplementary materials on Science Online.
10. J. J. Choi, X. Yang, Z. M. Norman, S. J. L. Billinge, J. S. Owen, Nano Lett. 14, 127–133 (2014).
11. J. R. Haynes, W. Shockley, Phys. Rev. 81, 835–843 (1951).
12. G. Giorgi, K. Yamashita, J. Mater. Chem. A 10.1039/C4TA05046K (2015).
13. E. Edri, S. Kirmayer, D. Cahen, G. Hodes, J. Phys. Chem. Lett. 4, 897–902 (2013).
14. M. A. Lampert, P. Mark, Current Injection in Solids (Academic Press, New York, 1970).
15. J. R. Ayres, J. Appl. Phys. 74, 1787–1792 (1993).
16. I. Capan, V. Borjanović, B. Pivac, Sol. Energy Mater. Sol. Cells 91, 931–937 (2007).
17. A. Balcioglu, R. K. Ahrenkiel, F. Hasoon, J. Appl. Phys. 88, 7175–7178 (2000).
18. L. L. Kerr et al., Solid-State Electron. 48, 1579–1586 (2004).
19. C. Goldmann et al., J. Appl. Phys. 99, 034507 (2006).
20. Y. S. Yang et al., Appl. Phys. Lett. 80, 1595–1597 (2002).
21. J. R. Haynes, J. A. Hornbeck, Phys. Rev. 100, 606–615 (1955).
22. J. A. Hornbeck, J. R. Haynes, Phys. Rev. 97, 311–321 (1955).

Supplementary Materials for

Low trap-state density and long carrier diffusion in organolead trihalide perovskite single crystals

Dong Shi, Valerio Adinolfi, Riccardo Comin, Mingjian Yuan, Erkki Alarousu, Andrei Buin, Yin Chen, Sjoerd Hoogland, Alexander Rothenberger, Khabiboulakh Katsiev, Yaroslav Losovyj, Xin Zhang, Peter A. Dowben, Omar F. Mohammed, Edward H. Sargent, Osman M. Bakr*

*Corresponding author. E-mail: osman.bakr@kaust.edu.sa

Published 30 January 2015, *Science* **347**, 519 (2015)
DOI: 10.1126/science.aaa2725

This PDF file includes:

Materials and Methods

Precursor Synthesis. The methylammonium halide precursors MAX (MA = $CH_3NH_3^+$, X = Br^- or I^-) were synthesized through the reaction of hydrohalide acid HX (X = Br or I) with methylamine followed by recrystallization from ethanol. An equimolar amount of HX acid solution in water was added dropwise into the methylamine (40% in methanol) at 0 °C under stirring. Then the mixture was stirred for 2 hours at 0 °C. Removal of the solvent was followed by recrystallization from ethanol to yield snow-white MAX crystals.

Thin Film Preparation. The crystalline $MAPbBr_3$ thin films deposited on glass substrate were prepared through a two-step solution processed procedure. *(6, 23)* A thin layer of $PbBr_2$ was initially coated onto the glass substrate by spin coating a solution of $PbBr_2$ in DMF ($100\ mg/mL$). The spin-coated $PbBr_2$ thin film was then annealed at 100 °C for 30 minutes. Subsequently, the as-annealed white $PbBr_2$ thin film was immersed into MABr solution in anhydrous isopropanol ($10\ mg/mL$) for 15 minutes at room temperature, which yielded a yellow thin film. Finally the as-obtained yellow thin film was gently rinsed with isopropanol and annealed at 80 °C for 1 hour.

Crystallization of $MAPbBr_3$. $PbBr_2$ and MABr (1/1 by molar, 0.2 M) were dissolved in N,N-dimethylformamide (DMF). MAPbBr3 single crystals were grown along with the slow diffusion of the vapor of the anti-solvent dichloromethane (DCM) in to the solution.

Crystallization of $MAPbI_3$. The same technique and anti-solvent for crystallizing $MAPbBr_3$ were used. PbI_2 and MAI (1/3 by molar, PbI_2: 0.5 M) were dissolved in gamma-butyrolactone (GBA).

Powder XRD characterization. $Cu\ K\alpha_1$ excitation ($E = 8047.8\ eV$) was employed for powder XRD measurements. Any remnant discrepancies in the relative peak intensities between the experimental and calculated powder XRD profiles stem from the specific surface orientation of the as-measured powders when exposed to the X-ray beam. ~ 50 pieces of crystals ranging from hundreds of micrometers to several millimeters were grounded into powder for powder XRD measurement to confirm the phase purity.

Single crystal X-ray diffraction. A small fraction ($\sim 0.1\ mm \times 0.1\ mm \times 0.1\ mm$) was cleaved from the as-grown $MAPbX_3$ (X = Br^- or I^-) crystals (Fig. S1). Data were collected on a STOE IPDS 2 diffractometer at 270 K using graphite-monochromated Mo-K_α radiation (λ = 0.71073 Å). For $MAPbBr_3$ single crystals, the unit cell was determined using 606 reflections from 48 measured frames (cubic, space group *P m3m* (no. 221), a = 5.9140(7) Å) confirming the single crystalline nature of the used material. The single crystalline nature was also established similarly for the as-grown $MAPbI_3$ single crystals (tetragonal, space group I 4/mcm, a = b = 8.8061 Å, c = 12.7019 Å). The crystal structure was refined using SHELXL-97 software. Detailed refinement parameters are given sections VI and VII.

Absorbance. The high transparency of the $MAPbBr_3$ single crystal enabled us to record its UV-Vis absorbance in transmission mode, while the colorless mother liquor did not absorb in the wavelength region defined in Fig. 2, and thus was used as a baseline reference for the absorption measurements. Storing the single crystals in the mother liquor also protects the surface from reconstructions caused by prolonged dewetting or exposure to air. The absorption of $MAPbI_3$ single crystal was recorded in reflection mode.

Time-dependent photoluminescence. Photoluminescence (PL) decay measurements were performed using a Horiba Fluorolog setup in reflection geometry. A transient population of carrier is impulsively excited in the sample (maintained in a dark environment) using an ultraviolet LED source ($\lambda = 355\,nm$, $\Delta t{\sim}0.7\,ns$) and a red laser diode ($\lambda = 633\,nm$, $\Delta t{\sim}0.8\,ns$) for $MAPbBr_3$ and $MAPbI_3$, respectively. The time-dependent photoluminescence signal is spectrally resolved using a single-grating spectrometer and acquired using a time-correlated detector operated in single-photon-counting mode. The presence of an impulsive, resolution-limited term in the time trace, is due to scattered laser light propagating in the spectrometer, and has been subtracted out in the analysis of carrier dynamics.

For the analysis of the time-resolved traces, multi-exponential profiles are used as trial fit functions. The metric used to assess the effectiveness of a particular type of fit function is the reduced chi-square χ^2_{red}, which allows comparing functions with different number of fit parameters on the same quantitative grounds:

$$\chi^2_{red} = \frac{1}{N-p-1}\sum_i \big(y_i - f(t_i)\big)^2$$

where y_i (t_i) are the experimental PL counts (time delays), $f(t)$ is the model fit function, N is the total number of points, and p is the number of free parameters. The model which minimizes the reduced chi-square is the one which attains the maximum likelihood of reproducing the experimental data.

An example of this procedure is shown in Fig. S4, which compares a bi- and tr-exponential fit on the $MAPbBr_3$ single crystal PL decay traces. The value of χ^2_{red} is lower for the bi-exponential fits, quantitatively demonstrating that a two-decay model is sufficient to reliably reproduce the experimental dataset.

Transient-absorption measurements. Nanosecond pump-probe TA spectroscopy was carried out using an EOS spectrometer to cover the ns to µs time window. The detailed experimental setup of EOS is provided elsewhere *(24)*. Briefly, we employed a white-light continuum probe pulse that was generated by a super continuum source. To generate the excitation pulse, 800 µJ of the Spitfire output is used to pump TOPAS-C two stage parametric amplifier equipped with frequency mixing stages and non-collinear difference frequency generator that allows tuning from 236 to 26000 nm. TOPAS-C output beam at 475 nm is routed via adjustable pinholes, variable neutral density filter, depolarizer, chopper wheel and focusing lens to excite the sample. Pump and probe beams are overlapping spatially and temporally in the sample. Finally, the absorbance change of the probe beam is collected by the ESO spectrometer to record the time-resolved TA spectra.

TOF carrier mobility. The Time-of-flight (TOF) technique relies on pulsed light excitation with energy larger than the material's bandgap i.e. $\hbar\omega > E_g$; an absorption depth much smaller than the sample thickness d; a transparent electrode allowing light illumination on one side; and an RC time constant of the detection circuitry much smaller than the transit time τ_t. The carrier mobility can be derived starting from its definition $v = \mu E$, where v is the carrier velocity, obtained from the ratio between the sample thickness and transit time ($v = d/\tau_t$), while the electric field is simply given by $E = V/d$. Altogether this leads to the formula $\mu = d^2/V\tau_t$, which is used to extract the mobility values in Fig. 3b

For this study, TOFmeasurements were performed using a Keithley 2400 as the power source and an Agilent infiniium DSO 8104A oscilloscope for acquiring the transient

signal. Monochromatic light excitation was provided by a pulsed laser at the wavelength of 355 nm. Pulses of 5 ns length at a frequency of 200 Hz were produced. The sample was kept in an enclosed, dark environment under vacuum at room temperature. A top transparent ITO and bottom MoO_3/Au/Ag stack electrode were utilized to apply the driving voltage that induces the charges to drift through the thickness of the crystal.

I-V measurements (SCLC). Current as a function of the applied voltage was measured using a Keithley Sub-femtoamp 6340, using a rather simple geometry with two electrodes on opposite sides of the sample, which is kept under vacuum ($p{\sim}10^{-4}\ mbar$) and in the dark. Ohmic contacts were deposited on opposite sides of the sample by consecutive thermal evaporation of MoO3, Au, and Ag. The sample was kept in a dark environment, under vacuum at monitored room temperature. A non-linear response was observed and analyzed according to SCLC theory. The link between the trap density and the onset voltage of the trap-filled-limit (TFL) regime is $V_{TFL} = en_t d^2/2\epsilon\epsilon_0$, where ϵ_0 is the vacuum permittivity *(14)*, while ϵ represents the material's dielectric constant – here we use $\epsilon = 25.5$ *(25)*.

Density Functional Theory (DFT). Calculations were performed within the Density Functional (DFT) formalism using the Perdew-Burke-Ernzerhof (PBE) *(26)* GGA exchange correlation functional. All calculations were performed utilizing the CP2K *(27)* package within Gaussian-augmented plane waves (GAPW) dual basis set using the molecular optimized double ζ-valence polarized (m-DZVP) *(27)* basis which have very small basis set superposition error (BSSE) *(28-31)*. The plane-wave cutoff was 300 Ry, which is suitable for the Goedecker-Teter-Hutter pseudopotentials *(32)*. Spin polarized (LSDA) and spin-unpolarized calculations (LDA) were performed in the case of the odd-even number of electrons. The structural minimization was performed with the help of the Broyden-Fletcher-Goldfarb-Shanno algorithm (BFGS) *(33)* in the case of the CP2K. Lattice constants were optimized and used throughout the calculations. The structural optimization was considered converged if the forces acting on the atoms were less than $0.04\ eV \cdot Å^{-1}$. CP2K is a Γ-point code, therefore a sufficient number of unit cells is required to guarantee the convergence. In our case, we have used 4 × 4 × 4 supercell of the original cubic unit cell for the defect calculations. Basis-set superposition error (BSSE) *(28, 34)* was estimated via the Counterpoise correction method *(35)* and found to be of the order of $50\ meV$ which is very small and was incorporated into final results. No spin-orbit coupling (SOC) has been taken into account, which was shown to be important *(36)* in calculating the bandstructure, however DFT-GGA calculations *(36-39)* without SOC effects were shown to capture semi-quantitative behaviour. In addition, SOC effects have been estimated to give small correction on the order of $0.25\ eV$ since defect formation energies are the ground state properties. Good agreement of the DFT bandgap between experiment and theory is largely attributed to large error cancellation *(36, 37)*. In the present manuscript we are mainly interested in the ground state properties, which are basically related to the valence band
manifold. The VBM and CBM character have been evaluated by density-of-states and wavefunction analysis.

The structural relaxation of the $MAPbBr_3$ cubic unit cell led to the lattice parameters being $a = b = c = 6.02$ Å, which is in a good agreement with previous results *(40)*. The calculated bandgap with these cell parameter is $E_g{\sim}2\ eV$ (see density of states plot in Fig. S9), which is in a good agreement with the experimental one (see Fig. 2A). Defect

formation energies computation procedure with all the corrections needed can be found elsewhere *(41)*.

Supplementary Text

The origins of low trap densities: insights from DFT. In order to understand the origins of the exceedingly low trap density observed experimentally, we carried out DFT simulations of the electronic structure of $MAPbBr_3$. Specifically, we examined defect formation energies under different growth conditions. The initial structure was relaxed, yielding a unit cell lattice parameter of $a = 6.02$ Å. The $MAPbBr_3$ formation energy, measured relative to its precursors MABr and $PbBr_2$, is found to be $-0.2\,eV$. This is larger (in magnitude) compared to $MAPbI_3$, likely explaining the higher stability of Br-based perovskite films. We computed the defect formation energies of all major deep defects under Br-rich (Fig. S9) and Br-poor (Fig. S10) growth conditions.

Under a Br-rich environment (shaded area) there is a wide range of possible Fermi levels (i.e. of doping values) that are free of deep traps, because of the high formation energies of the latter. In contrast, in the case of a Br-poor/Pb-rich environment, this region is limited to the p-side and is a much narrower window. It is therefore preferable to grow the perovskite under Br-rich condition in order to have a wide process window for trap-free bromide perovskites.

We also calculated the binding energies of various complex defects, such as: (i) antisites A_B (B occupying the atomic position of A); (ii) vacancies V_A (missing A species); (iii) interstitials A_i (species A found at a forbidden location in the lattice).

The binding energies of Pb_{Br} and Br_{Pb} antisites at various charged states are given by *(42)*:

$$E_b[(\mathrm{V_{Pb}} + \mathrm{Br_i})^q] = E_f\left[\mathrm{Pb_{Br}^q}\right] - E_f[\mathrm{V_{Pb}^n}] - E_f[\mathrm{Br_i^m}]$$

$$E_b[(\mathrm{V_{Br}} + \mathrm{Pb_i})^q] = E_f\left[\mathrm{Br_{Pb}^q}\right] - E_f[\mathrm{V_{Br}^n}] - E_f[\mathrm{Pb_i^m}]$$

where E_b is the defect binding energy, whereas E_f is the defect formation energy of the various defects with q, m, n charged states ($q = m + n$). The binding energies are given below, in eV (negative means stable, positive means unstable):

$$E_b\left(\mathrm{Pb_{Br}^0} \rightarrow \mathrm{V_{Pb}^0} + \mathrm{Br_i^0}\right) = 0.20745$$
$$E_b\left(\mathrm{Pb_{Br}^{-3}} \rightarrow \mathrm{V_{Pb}^{-2}} + \mathrm{Br_i^{-1}}\right) = 2.3584$$
$$E_b\left(\mathrm{Pb_{Br}^{-2}} \rightarrow \mathrm{V_{Pb}^{-1}} + \mathrm{Br_i^{-1}}\right) = 1.1668$$
$$E_b\left(\mathrm{Pb_{Br}^{-2}} \rightarrow \mathrm{V_{Pb}^{-2}} + \mathrm{Br_i^0}\right) = 2.3739$$
$$E_b\left(\mathrm{Pb_{Br}^{-1}} \rightarrow \mathrm{V_{Pb}^{-1}} + \mathrm{Br_i^0}\right) = -0.45095$$
$$E_b\left(\mathrm{Pb_{Br}^{-1}} \rightarrow \mathrm{V_{Pb}^{-2}} + \mathrm{Br_i^{+1}}\right) = 1.8364$$
$$E_b\left(\mathrm{Pb_{Br}^{-1}} \rightarrow \mathrm{V_{Pb}^0} + \mathrm{Br_i^{-1}}\right) = -0.2093$$
$$E_b\left(\mathrm{Br_{Pb}^0} \rightarrow \mathrm{V_{Br}^0} + \mathrm{Pb_i^0}\right) = 1.2946$$
$$E_b\left(\mathrm{Br_{Pb}^{+3}} \rightarrow \mathrm{V_{Br}^{+1}} + \mathrm{Pb_i^{+2}}\right) = 1.3297$$
$$E_b\left(\mathrm{Br_{Pb}^{+2}} \rightarrow \mathrm{V_{Br}^{+1}} + \mathrm{Pb_i^{+1}}\right) = 1.7364$$
$$E_b\left(\mathrm{Br_{Pb}^{+2}} \rightarrow \mathrm{V_{Br}^0} + \mathrm{Pb_i^{+2}}\right) = 0.62092$$
$$E_b\left(\mathrm{Br_{Pb}^{+1}} \rightarrow \mathrm{V_{Br}^0} + \mathrm{Pb_i^{+1}}\right) = 1.5627$$
$$E_b\left(\mathrm{Br_{Pb}^{+1}} \rightarrow \mathrm{V_{Br}^{+1}} + \mathrm{Pb_i^0}\right) = 1.2593$$

The only complex which appears to be stable is Pb_{Br}^{-1}, which however is prone to decompose into the most stable V_{Pb}^{-2} and Br_i^{+1} defects. Ultimately, no complexes are found to be stable, since Pb_{Br} always decomposes into lead vacancy (V_{Pb}) and Br-interstitial (Br_i), while Br_{Pb} always decomposes into the bromide vacancy (V_{Br}) and Pb-interstitial (Pb_i). While the formation of Pb_{Br} and Br_{Pb} antisites during growth is not prevented *a priori*, such defects tend to decompose under energy-activating mechanisms such as annealing or light soaking. Br_i in the oxidation state +1 has a very narrow stability region which only occurs for strongly p-type crystals, and thus singles out Pb_i as the only major deep defect. This defect has a higher formation energy in the case of Br-rich than for Br-poor synthesis (see Fig. S9 and S10), yielding a final lower density of trap states in the former case. One way to control the richness/poorness of the growth environment is to choose a lead precursor that brings with it an excess of bromide: $PbBr_2$, as used in the present work. Altogether, the DFT calculations of formation energies of the major defect states in $MAPbBr_3$ confirms that a Br-rich synthesis leads to a low trap density, as observed experimentally.

Single Crystal XRD data of $MAPbBr_3$.

```
TITL ds1a in Pm-3m
CELL 1.54178   5.9215   5.9215   5.9215  90.000  90.000  90.000
ZERR    1.00   0.0001   0.0001   0.0001   0.000   0.000   0.000
LATT  1
SYMM -X, -Y, Z
SYMM -X, Y, -Z
SYMM X, -Y, -Z
SYMM Z, X, Y
SYMM Z, -X, -Y
SYMM -Z, -X, Y
SYMM -Z, X, -Y
SYMM Y, Z, X
SYMM -Y, Z, -X
SYMM Y, -Z, -X
SYMM -Y, -Z, X
SYMM Y, X, -Z
SYMM -Y, -X, -Z
SYMM Y, -X, Z
SYMM -Y, X, Z
SYMM X, Z, -Y
SYMM -X, Z, Y
SYMM -X, -Z, -Y
SYMM X, -Z, Y
SYMM Z, Y, -X
SYMM Z, -Y, X
SYMM -Z, Y, X
SYMM -Z, -Y, -X
SFAC C H N BR PB
UNIT 1 6 1 3 1

L.S. 100
BOND
FMAP 2
PLAN 5
temp 23
size 0.2 0.2 0.2
```

```
acta 50

dfix -1.711 c1 n1

WGHT    0.059200
FVAR       0.67130
PB1    5     0.500000     0.500000     0.500000     10.02083     0.02191
0.02191 =
         0.02191    0.00000    0.00000    0.00000
BR1    4     0.000000     0.500000     0.500000     10.06250     0.01895
0.13562 =
         0.13562    0.00000    0.00000    0.00000
C1    1    0.092303    0.000000    0.000000    10.02082    0.03822
N1    3    0.000000    0.192931    0.192931    10.02082    0.13341
HKLF 4

REM  ds1a in Pm-3m
REM R1 =  0.0349 for      68 Fo > 4sig(Fo)  and  0.0349 for all      68
data
REM      8 parameters refined using      1 restraints

END

WGHT      0.0619      0.5706
REM Highest difference peak   0.875,   deepest hole  -2.132,   1-sigma
level  0.616
Q1    1   0.2476  0.3359  0.3359  10.50000  0.05    0.88
Q2    1   0.2104  0.5000  0.2104  10.25000  0.05    0.67
Q3    1   0.2066  0.0000  0.0000  10.12500  0.05    0.39
Q4    1   0.0000  0.1254  0.1254  10.25000  0.05    0.38
```

Single crystal XRD data of $MAPbI_3$

```
TITL bo2941-1 in I4/m
CELL 0.71073   8.8061   8.8061  12.7019  90.000  90.000  90.000
ZERR   12.00   0.0005   0.0005   0.0014   0.000   0.000   0.000
LATT  2
SYMM -X, -Y, Z
SYMM -Y, X, Z
SYMM Y, -X, Z
SFAC C H O I PB N
UNIT 12 12 12 12 1 1
TEMP -80
SIZE .155 .145 .115
ACTA
CONF
OMIT 0 3 1
OMIT 0 1 3
OMIT 1 1 2
L.S. 6
BOND $H
FMAP 2
PLAN 9
WGHT    0.056100    0.633000
EXTI    0.003814
FVAR       0.13693
```

```
PB1    5     0.000000     0.000000     0.000000     10.12500     0.02179
0.02179 =
         0.02256    0.00000    0.00000    0.00000
PB2    5     0.000000     0.000000     0.500000     10.12500     0.02180
0.02180 =
         0.02311    0.00000    0.00000    0.00000
I1     4     0.000000     0.000000     0.250143     10.25000     0.05775
0.05775 =
         0.01697    0.00000    0.00000    0.00000
I2     4    -0.201142    -0.298834     0.000000     10.50000     0.04008
0.04151 =
         0.06486    0.00000    0.00000   -0.02533
HKLF 4

REM  bo2941-1 in I4/m
REM R1 =  0.0569 for     581 Fo > 4sig(Fo)  and  0.0764 for all     846
data
REM     15 parameters refined using      0 restraints

END

WGHT      0.0473      0.0000
REM Highest difference peak   4.228,   deepest hole  -2.049,   1-sigma
level  0.553
Q1    1  -0.2581 -0.2451 -0.0396  11.00000  0.05    4.23
Q2    1   0.0000 -0.5000  0.0000  10.25000  0.05    2.71
Q3    1   0.0013  0.4122  0.2503  11.00000  0.05    1.91
Q4    1   0.0747  0.0662  0.2247  11.00000  0.05    1.81
Q5    1   0.1770  0.2023  0.2504  11.00000  0.05    1.79
Q6    1   0.0647  0.0780  0.2818  11.00000  0.05    1.79
Q7    1   0.0601  0.0466  0.4552  11.00000  0.05    1.75
Q8    1   0.0589  0.0482  0.0444  11.00000  0.05    1.70
Q9    1   0.0000  0.0000  0.1609  10.25000  0.05    1.66
```

Author Contributions. D.S. conceived the idea, proposed the research, optimized the crystallization procedures, measured the powder XRD, UV-Vis, and PL and analyzed the data. V.A., R.C., S.H., M.Y., A.B. and E.H.S. designed, performed, and analyzed the measurements of mobility, PL lifetime, I-V trap-state density, and DFT calculation. Y.C. assisted with the precursor's synthesis. E.A. and O.F.M. conducted and analyzed the TA measurement. A.R. and Y.C. conducted single crystal XRD characterization and data-analysis. O.M.B. crafted and directed the overall research plan. D.S., V.A., R.C., E.H.S., and O.M.B. co-wrote the manuscript. All authors read and commented on the manuscript.

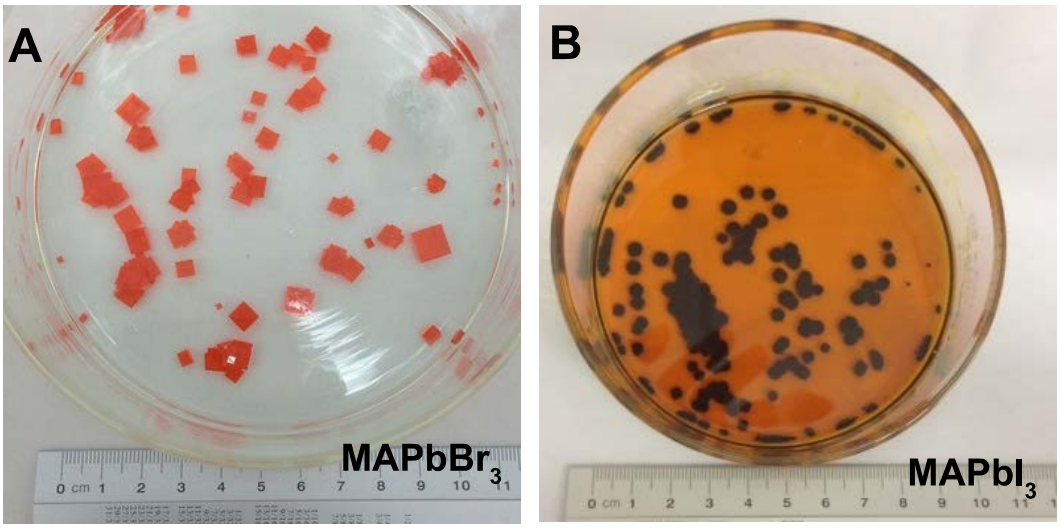

Figure S1. Photograph of a batch of the as-grown $MAPbBr_3$ and $MAPbI_3$ single crystals obtained within one week.

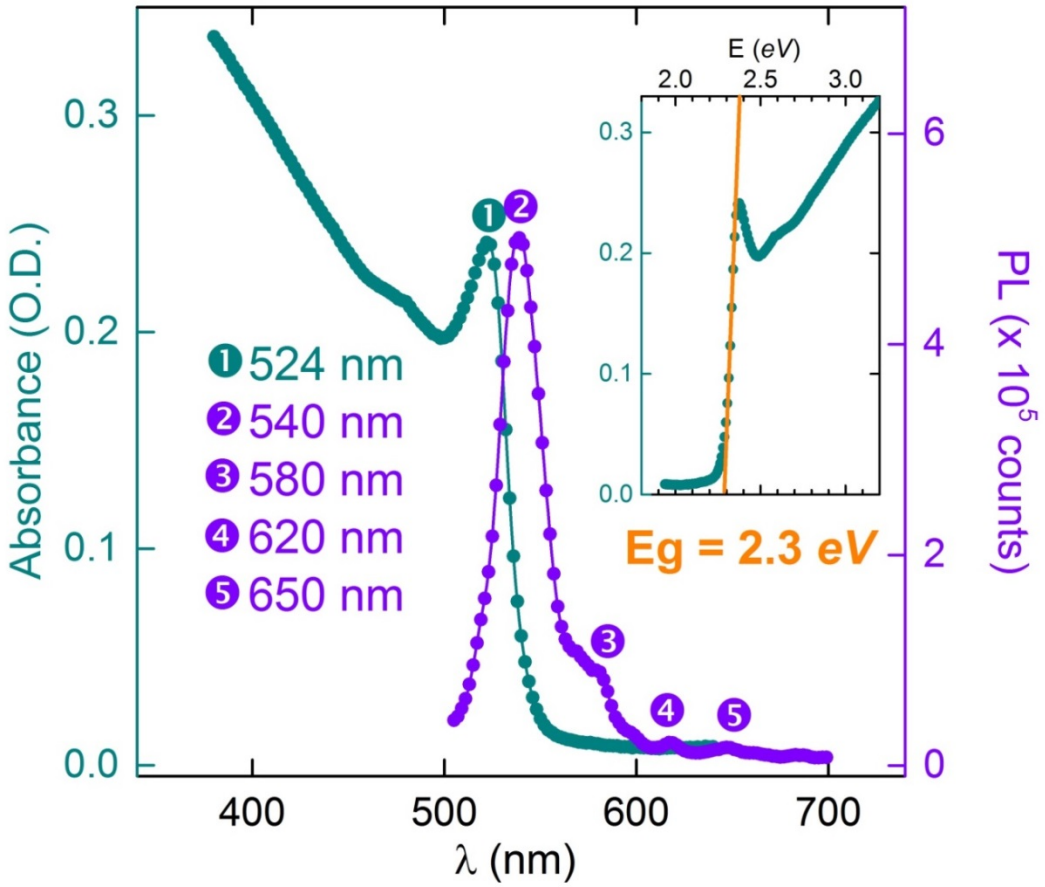

Figure S2. A: Static absorbance and PL spectrum of $MAPbI_3$ thin films. Excitation wavelength of 480 nm was used to record the PL.
The main peak occurring at 540 nm in thin films may stem from the low-dimensional structurally coherent units within the $MAPbBr_3$ film, whereas the noticeable peak at longer wavelength around 580 nm may be attributed to the intrinsic PL of the fully crystallized three-dimensional $MAPbBr_3$ lattice which is less tight in thin films than in single crystals. Other PL signals appearing around 620 nm and 650 nm may originate from sub gap trap states *(43)*.

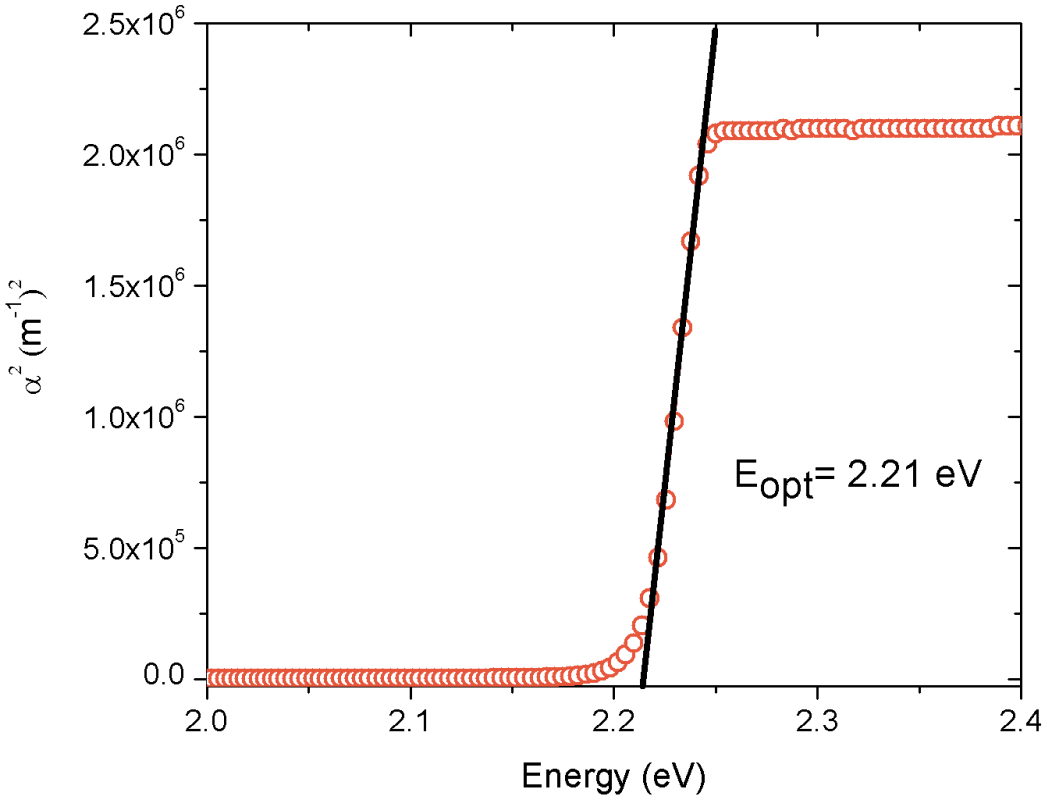

Figure S3. Extraction of the optical band gap of $MAPbBr_3$ single crystal.
The optical bandgap is extracted by using the relation:

$$\alpha = c\,(hf\text{-}E_g)^{1/2} \qquad (44)$$

Where *hf* is the photon energy, α is the optical absorption coefficient, E_g the energy bandgap and c a constant of the material. The exponent 1/2 in the right side of the equation applies for direct bandgap semiconductors. The measured bandgap, 2.21 eV, is in good agreement with the DFT computed value (2.2 eV) shown in Fig. S11.

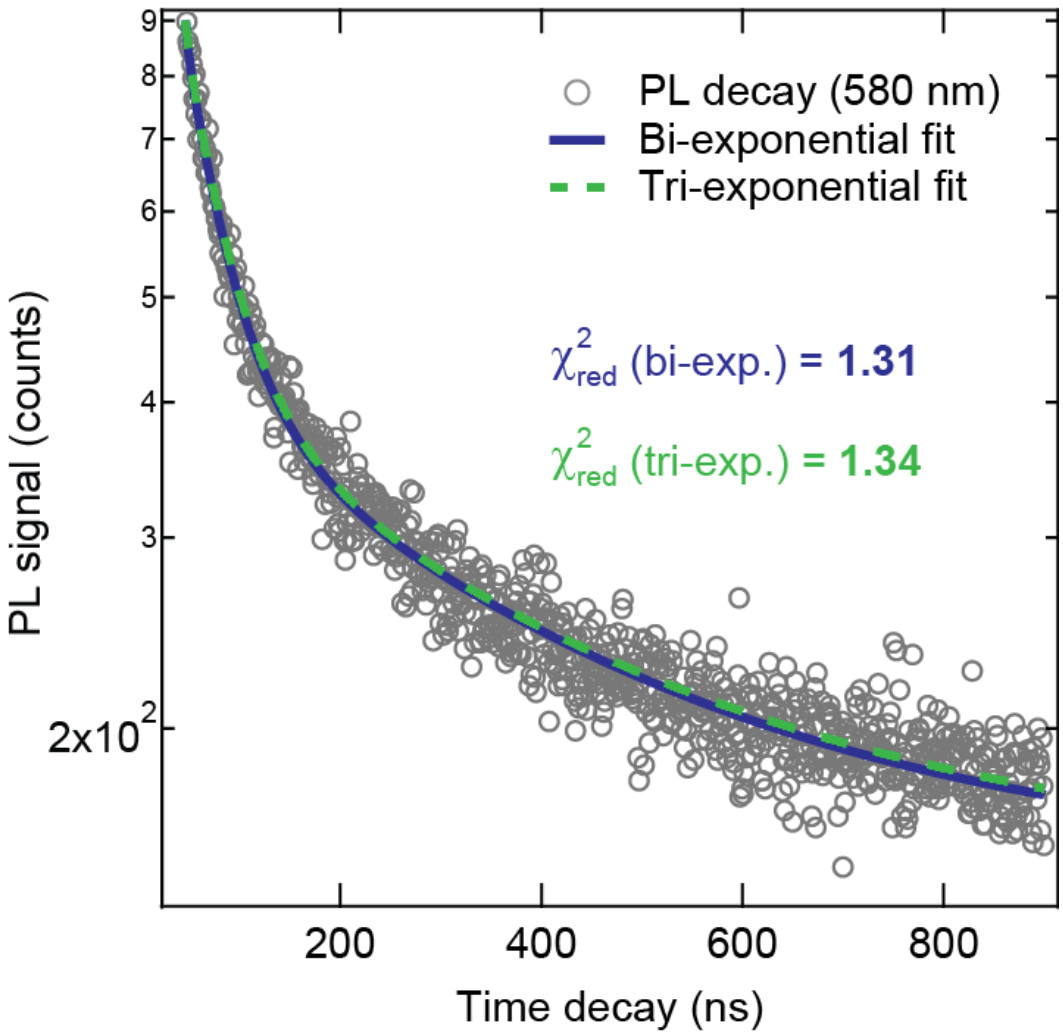

Figure S4. Model comparison for the analysis of the PL decay time traces on a MAPbBr3 single crystalline sample. Overlaid on top of the experimental PL decay trace (grey markers, same as Fig. 3) are plotted the bi-exponential (blue) and tri-exponential (green) fit profiles. The values of the reduced chi-square χ^2_{red} for the two models are also reported, demonstrating that a tri-exponential model does not perform better than a bi-exponential one.

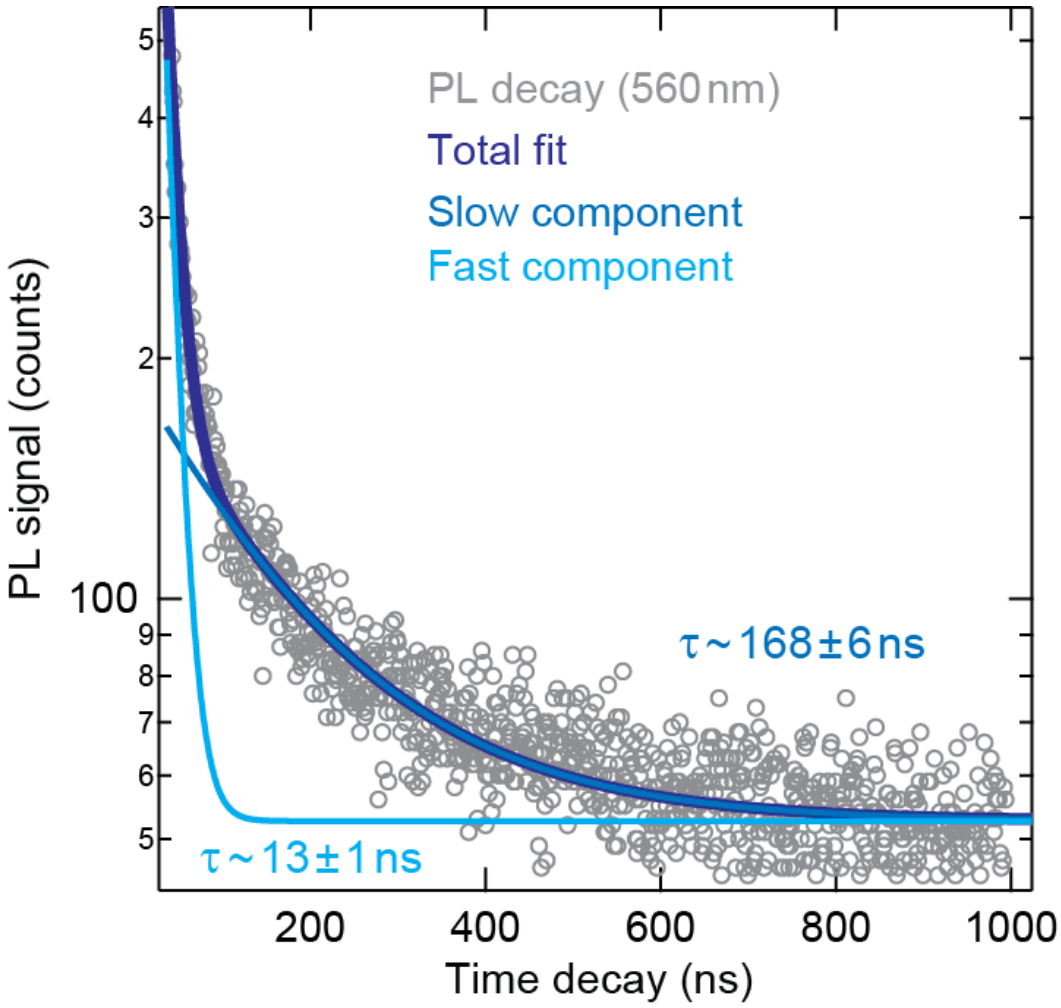

Figure S5. Time-resolved PL of $MAPbBr_3$ thin films, acquired at $\lambda = 560\ nm$, showing the experimental time trace (grey markers) with bi-exponential fit (continuous lines) and corresponding time constants superimposed.

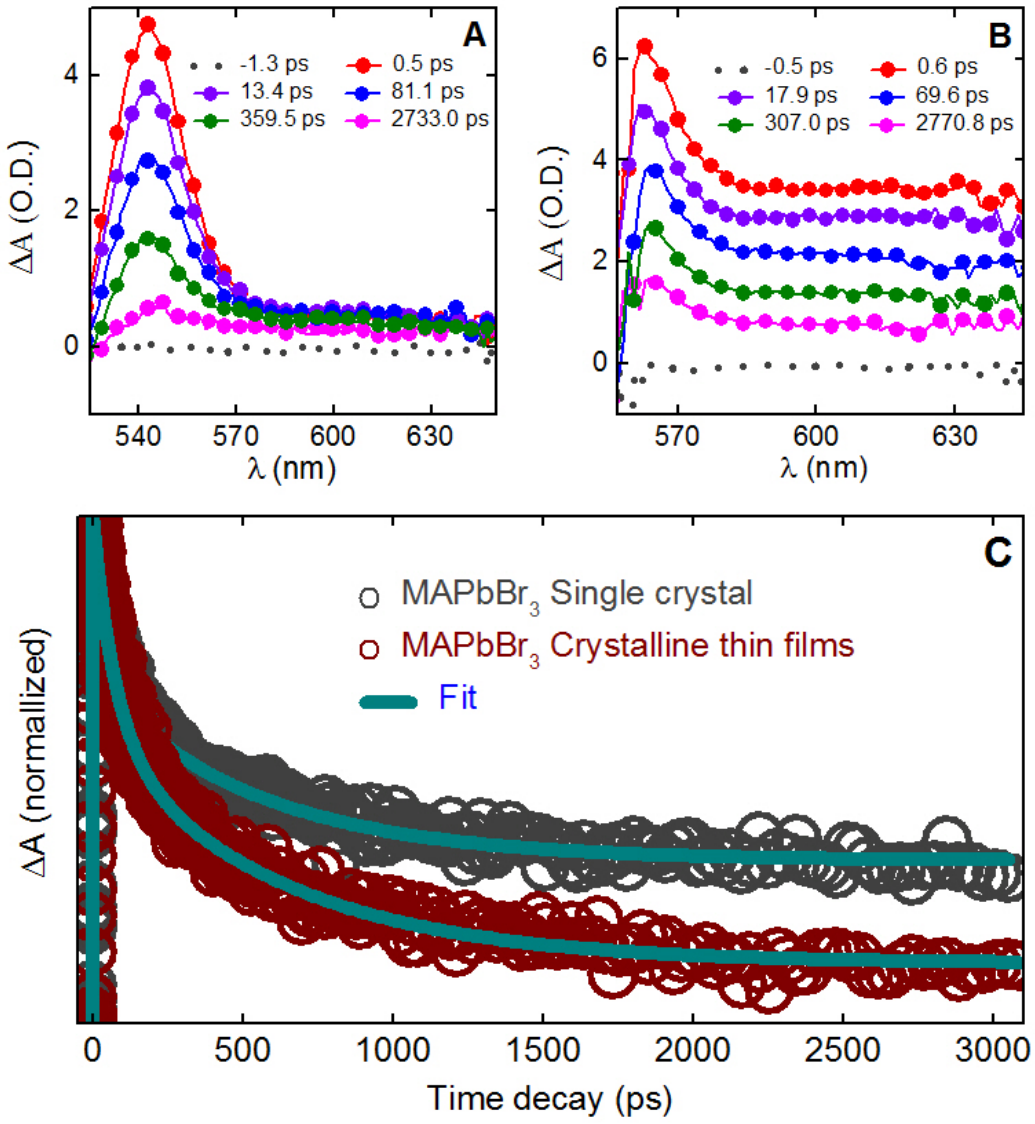

Figure S6: Transient absorption. Transient absorption spectra of the thin film (A) and single crystal (B) of $MAPbBr_3$. (C) The normalized time profile of transient absorption of the thin film (red dots) and single crystal (black dots) of $MAPbBr_3$ Measured at 480 nm excitation. The solid line is the calculated signal.

As can be clearly seen in Fig. S6, under the same experimental conditions, the decay of the excited state due to the electron hole recombination of single crystals is much longer than the thin film (Fig. S6C). The observed decay can be attributed to trap-assisted recombination of charge carriers, indicating that substantially fewer defect trap-states are present in the single crystal relative to the thin film. This finding is consistent with the long carrier lifetimes extracted from photoluminescence experiments on single crystals.

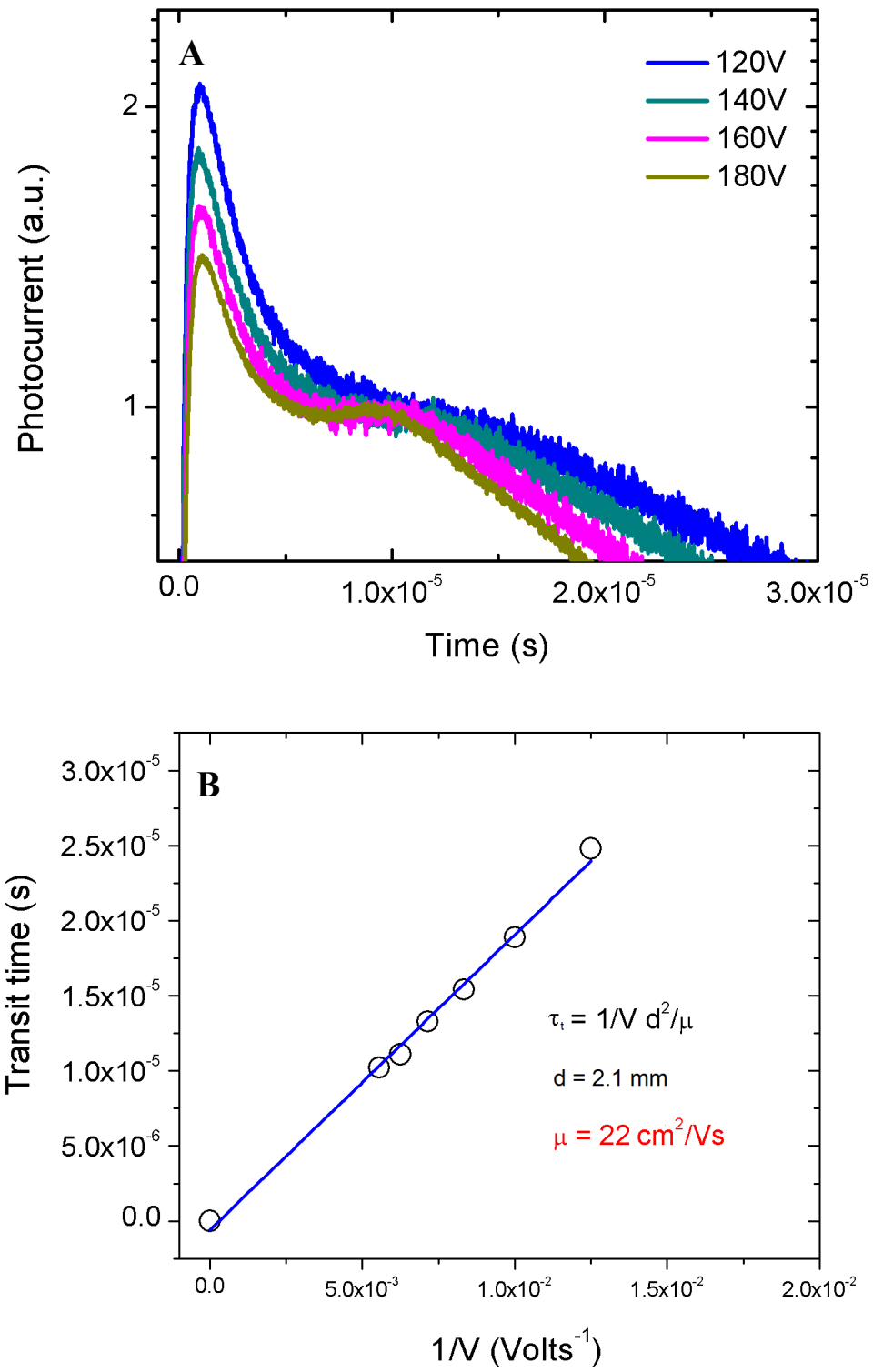

Fig. S7. A: Time of flight measurements, on $MAPbBr_3$, B: Lower mobility are shown for completeness. A small variability between the samples is seen.

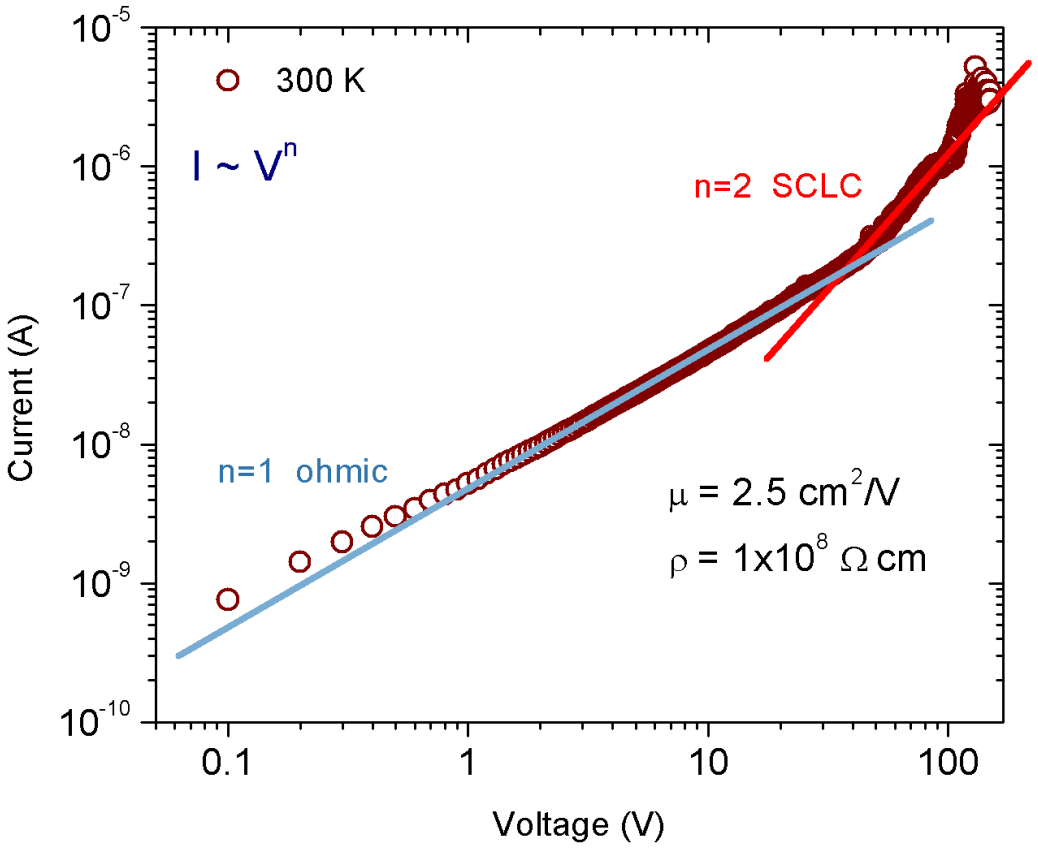

Figure S8. Space Charge limited Current analysis for a $MAPbI_3$ single crystal of dimensions: 1.63 mm x 2.74 mm x 2.74 mm.

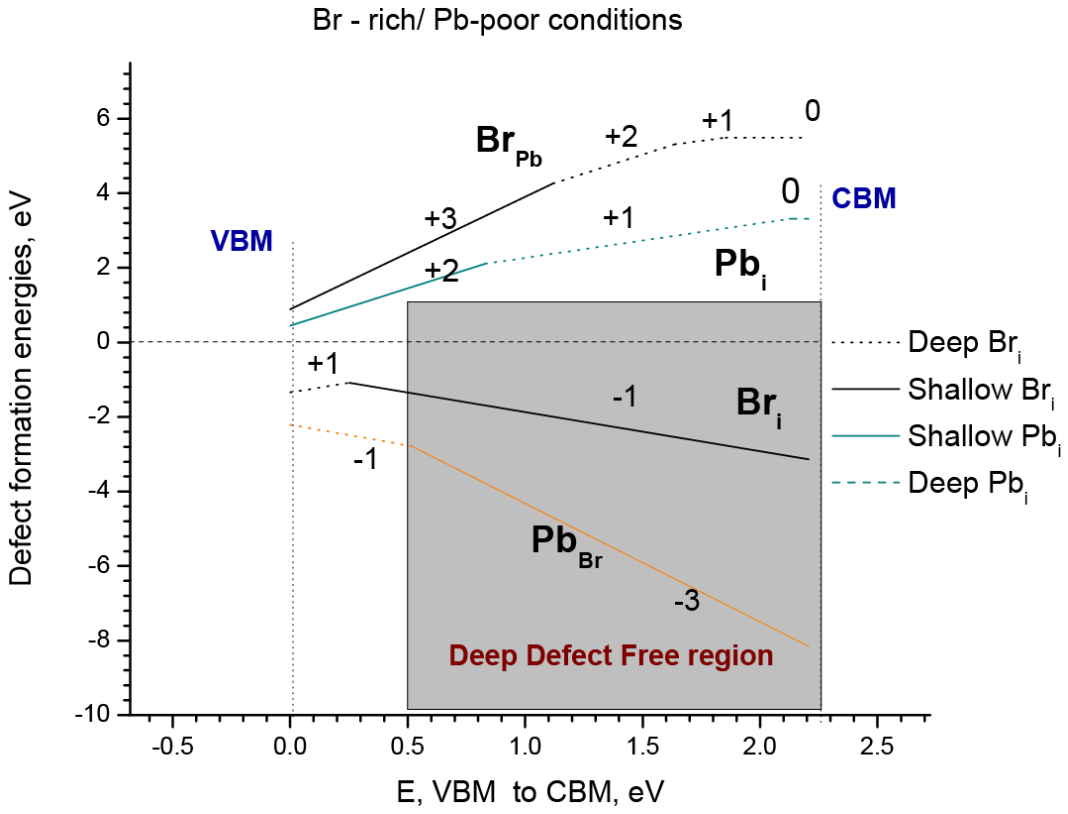

Figure S9. Defect formation energies in case of Br-rich growth conditions. No vacancies are displayed due to their shallow nature.

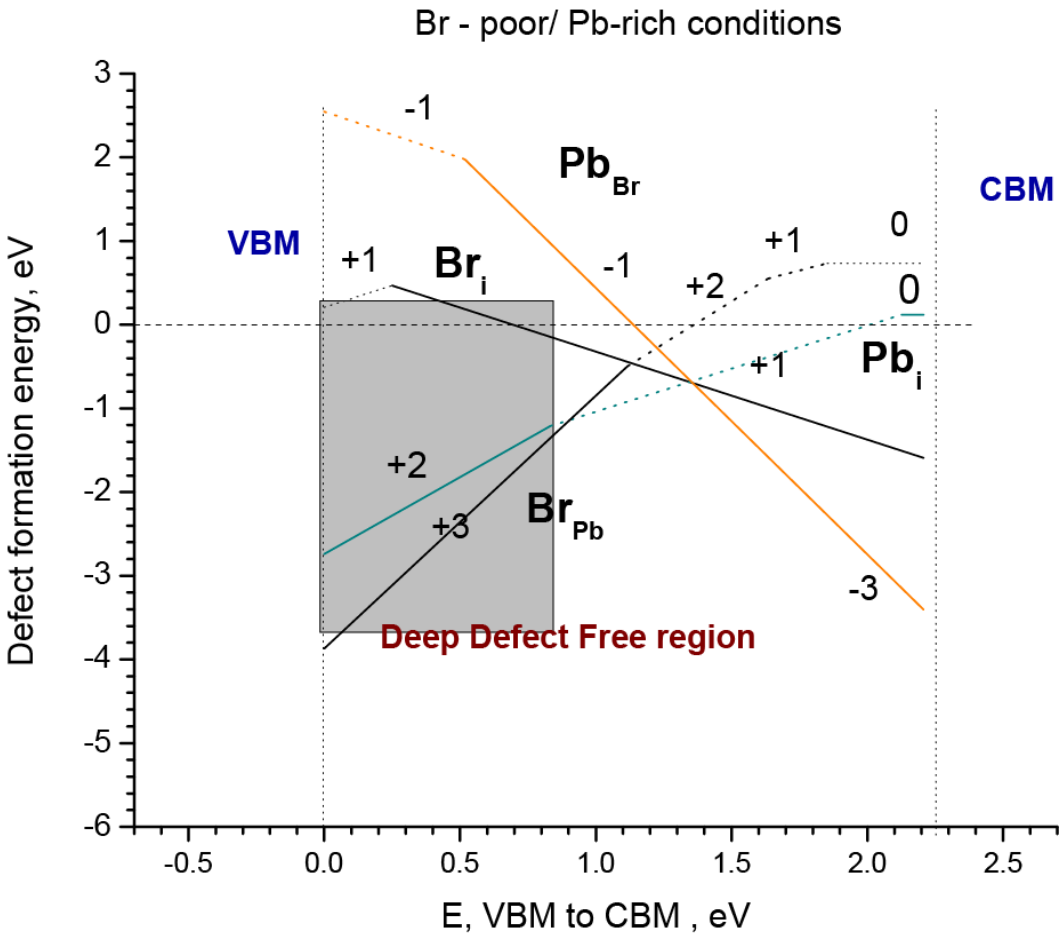

Figure S10. Defect formation energies in case of Br-poor growth conditions. No vacancies are displayed due to their shallow nature.

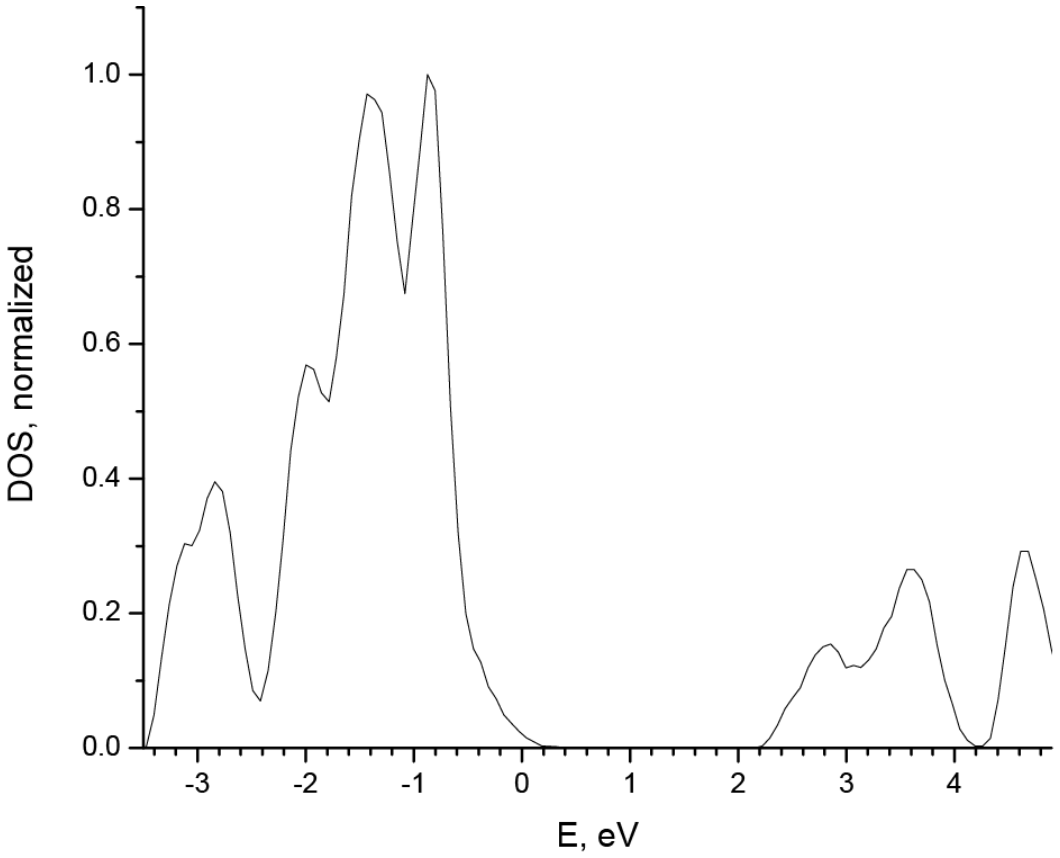

Figure S11. $MAPbBr_3$ Density of States (DOS).

Nanometrics HL5500 Hall System
Measured on 10/28/14 at 2:07 PM

SPECIMEN
Wafer ID: 1
Batch ID: 1
Material: MAPbBr3
Description:
Thickness: 2000.000 µm

MEASURING CONDITIONS
I-meas: 3.8 nA DC
Temperature: 296.6
Field: 0.504 Tesla

Targ.Vr: 200 mV

RESULTS SUMMARY

Rs: 1.859e+08 ohm/sq	RHs: +5.27e+05 m²/C	Ns: +1.184e+09 /cm²
R : 3.718e+07 ohm-cm	Mob: 28.3 cm²/V-s	N : +5.922e+09 /cm³

CONTACT CHECK

Pair	M-ohms
12	1.7e+02
23	1.5e+02
34	1.6e+02
41	1.3e+02
13	1.9e+02
24	1.8e+02

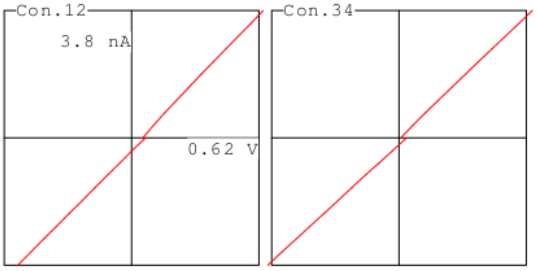

RESISTIVITY

Meas	+++	Vm	---	Sym	Factor	R-sheet
43	+2.204e-01	-1.779e-01		1.70	0.98	1.841e+08
41	+1.291e-01	-1.052e-01		1.73	0.97	1.861e+08
21	+1.792e-01	-2.271e-01		1.70	0.98	1.877e+08
23	+9.679e-02	-1.417e-01		1.67	0.98	1.856e+08

HALL MEASUREMENTS

	+++	24	---	+++	13	---
Misalignment	-5.85e-02	-7.08e-02		+1.25e-02	+2.40e-02	
Offset applied		-3.33e-03			+5.67e-03	
V-hall North	-6.10e-02	-6.55e-02		+1.62e-02	+1.68e-02	
V-hall South	-5.74e-02	-6.16e-02		+1.31e-02	+1.39e-02	
V-hall (mean)		+7.66e-05			+5.89e-05	
V-hall (over all cycles)			+6.77e-05			

Figure S12. Hall effect results.

References

1. National Renewable Energy Laboratory, Research Cell Efficiency Records Chart; www.nrel.gov/ncpv/images/efficiency_chart.jpg.

2. A. Kojima, K. Teshima, Y. Shirai, T. Miyasaka, Organometal halide perovskites as visible-light sensitizers for photovoltaic cells. *J. Am. Chem. Soc.* **131**, 6050–6051 (2009). Medline doi:10.1021/ja809598r

3. T. C. Sum, N. Mathews, Advancements in perovskite solar cells: Photophysics behind the photovoltaics. *Energy Environ. Sci.* **7**, 2518–2534 (2014). doi:10.1039/C4EE00673A

4. C. Wehrenfennig, M. Liu, H. J. Snaith, M. B. Johnston, L. M. Herz, Charge-carrier dynamics in vapour-deposited films of the organolead halide perovskite $CH_3NH_3PbI_{3-x}Cl_x$. *Energy Environ. Sci.* **7**, 2269–2275 (2014). doi:10.1039/c4ee01358a

5. S. D. Stranks, G. E. Eperon, G. Grancini, C. Menelaou, M. J. P. Alcocer, T. Leijtens, L. M. Herz, A. Petrozza, H. J. Snaith, Electron-hole diffusion lengths exceeding 1 micrometer in an organometal trihalide perovskite absorber. *Science* **342**, 341–344 (2013). Medline doi:10.1126/science.1243982

6. D. B. Mitzi, Synthesis, structure, and properties of organic-inorganic perovskites and related materials. *Prog. Inorg. Chem.* **48**, 1–121 (1999). doi:10.1002/9780470166499.ch1

7. Y. Tidhar, E. Edri, H. Weissman, D. Zohar, G. Hodes, D. Cahen, B. Rybtchinski, S. Kirmayer, Crystallization of methyl ammonium lead halide perovskites: Implications for photovoltaic applications. *J. Am. Chem. Soc.* **136**, 13249–13256 (2014). Medline doi:10.1021/ja505556s

8. M. Xiao, F. Huang, W. Huang, Y. Dkhissi, Y. Zhu, J. Etheridge, A. Gray-Weale, U. Bach, Y.-B. Cheng, L. Spiccia, A fast deposition-crystallization procedure for highly efficient lead iodide perovskite thin-film solar cells. *Angew. Chem. Int. Ed.* **53**, 9898–9903 (2014). Medline doi:10.1002/anie.201405334

9. See supplementary materials on *Science* Online.

10. J. J. Choi, X. Yang, Z. M. Norman, S. J. L. Billinge, J. S. Owen, Structure of methylammonium lead iodide within mesoporous titanium dioxide: Active material in

high-performance perovskite solar cells. *Nano Lett.* **14**, 127–133 (2014). Medline doi:10.1021/nl403514x

11. J. R. Haynes, W. Shockley, The mobility and life of injected holes and electrons in germanium. *Phys. Rev.* **81**, 835–843 (1951). doi:10.1103/PhysRev.81.835

12. G. Giorgi, K. Yamashita, Organic-inorganic halide perovskites: An ambipolar class of materials with enhanced photovoltaic performances. *J. Mater. Chem. A* 10.1039/C4TA05046K (2015). doi:10.1039/C4TA05046K

13. E. Edri, S. Kirmayer, D. Cahen, G. Hodes, High open-circuit voltage solar cells based on organic–inorganic lead bromide perovskite. *J. Phys. Chem. Lett.* **4**, 897–902 (2013). doi:10.1021/jz400348q

14. M. A. Lampert, P. Mark, *Current Injection in Solids* (Academic Press, New York, 1970).

15. J. R. Ayres, Characterization of trapping states in polycrystalline-silicon thin film transistors by deep level transient spectroscopy. *J. Appl. Phys.* **74**, 1787–1792 (1993). doi:10.1063/1.354782

16. I. Capan, V. Borjanović, B. Pivac, Dislocation-related deep levels in carbon rich p-type polycrystalline silicon. *Sol. Energy Mater. Sol. Cells* **91**, 931–937 (2007). doi:10.1016/j.solmat.2007.02.011

17. A. Balcioglu, R. K. Ahrenkiel, F. Hasoon, Deep-level impurities in CdTe/CdS thin-film solar cells. *J. Appl. Phys.* **88**, 7175–7178 (2000). doi:10.1063/1.1326465

18. L. L. Kerr, S. S. Li, S. W. Johnston, T. J. Anderson, O. D. Crisalle, W. K. Kim, J. Abushama, R. N. Noufi, *Solid-State Electron.* **48**, 1579–1586 (2004). doi:10.1016/j.sse.2004.03.005

19. C. Goldmann, C. Krellner, K. P. Pernstich, S. Haas, D. J. Gundlach, B. Batlogg, Determination of the interface trap density of rubrene single-crystal field-effect transistors and comparison to the bulk trap density. *J. Appl. Phys.* **99**, 034507 (2006). doi:10.1063/1.2170421

20. Y. S. Yang, S. H. Kim, J.-I. Lee, H. Y. Chu, L.-M. Do, H. Lee, J. Oh, T. Zyung, M. K. Ryu, M. S. Jang, Deep-level defect characteristics in pentacene organic thin films. *Appl. Phys. Lett.* **80**, 1595–1597 (2002). doi:10.1063/1.1459117

21. J. R. Haynes, J. A. Hornbeck, Trapping of minority carriers in silicon. II. n-type silicon. *Phys. Rev.* **100**, 606–615 (1955). doi:10.1103/PhysRev.100.606

22. J. A. Hornbeck, J. R. Haynes, Trapping of minority carriers in silicon. I. p-type silicon. *Phys. Rev.* **97**, 311–321 (1955). doi:10.1103/PhysRev.97.311

23. J. Burschka, N. Pellet, S.-J. Moon, R. Humphry-Baker, P. Gao, M. K. Nazeeruddin, M. Grätzel, Sequential deposition as a route to high-performance perovskite-sensitized solar cells. *Nature* **499**, 316–319 (2013). Medline doi:10.1038/nature12340

24. A. O. El-Ballouli, E. Alarousu, M. Bernardi, S. M. Aly, A. P. Lagrow, O. M. Bakr, O. F. Mohammed, Quantum confinement-tunable ultrafast charge transfer at the PbS quantum dot and phenyl-C_{61}-butyric acid methyl ester interface. *J. Am. Chem. Soc.* **136**, 6952–6959 (2014). Medline doi:10.1021/ja413254g

25. A. Poglitsch, D. Weber, Dynamic disorder in methylammoniumtrihalogenoplumbates (II) observed by millimeter-wave spectroscopy. *J. Chem. Phys.* **87**, 6373–6378 (1987). doi:10.1063/1.453467

26. J. P. Perdew, K. Burke, M. Ernzerhof, Generalized gradient approximation made simple. *Phys. Rev. Lett.* **77**, 3865–3868 (1996). Medline doi:10.1103/PhysRevLett.77.3865

27. J. VandeVondele, J. Hutter, Gaussian basis sets for accurate calculations on molecular systems in gas and condensed phases. *J. Chem. Phys.* **127**, 114105 (2007). Medline doi:10.1063/1.2770708

28. R. Leitsmann, O. Böhm, P. Plänitz, C. Radehaus, M. Schaller, M. Schreiber, Adsorption mechanisms of fluorocarbon polymers at ultra low-k surfaces. *Surf. Sci.* **604**, 1808–1812 (2010). doi:10.1016/j.susc.2010.07.011

29. T. T. Takaluoma, K. Laasonen, R. S. Laitinen, Molecular dynamics simulation of the solid-state topochemical polymerization of S_2N_2. *Inorg. Chem.* **52**, 4648–4657 (2013). Medline doi:10.1021/ic400273p

30. N. Bork, V. Loukonen, H. Vehkamäki, Reactions and reaction rate of atmospheric SO_2 and $O_3^-(H_2O)_n$ collisions via molecular dynamics simulations. *J. Phys. Chem. A* **117**, 3143–3148 (2013). Medline doi:10.1021/jp311103z

31. E. Smecca, A. Motta, M. E. Fragalà, Y. Aleeva, G. G. Condorelli, Spectroscopic and theoretical study of the grafting modes of phosphonic acids on ZnO nanorods. *J. Phys. Chem. C* **117**, 5364–5372 (2013). doi:10.1021/jp308983p

32. C. Hartwigsen, S. Goedecker, J. Hutter, Relativistic separable dual-space Gaussian pseudopotentials from H to Rn. *Phys. Rev. B* **58**, 3641–3662 (1998). doi:10.1103/PhysRevB.58.3641

33. W. H. Press, *Numerical Recipes: The Art of Scientific Computing* (Cambridge Univ. Press, Cambridge, ed. 3, 2007.

34. H. B. Jansen, P. Ros, Non-empirical molecular orbital calculations on the protonation of carbon monoxide. *Chem. Phys. Lett.* **3**, 140–143 (1969). doi:10.1016/0009-2614(69)80118-1

35. S. F. Boys, F. Bernardi, The calculation of small molecular interactions by the differences of separate total energies. Some procedures with reduced errors. *Mol. Phys.* **19**, 553–566 (1970). doi:10.1080/00268977000101561

36. J. Even, L. Pedesseau, J.-M. Jancu, C. Katan, Importance of spin-orbit coupling in hybrid organic/inorganic perovskites for photovoltaic applications. *J. Phys. Chem. Lett.* **4**, 2999–3005 (2013). doi:10.1021/jz401532q

37. E. Mosconi, A. Amat, M. K. Nazeeruddin, M. Grätzel, F. De Angelis, First-principles modeling of mixed halide organometal perovskites for photovoltaic applications. *J. Phys. Chem. C* **117**, 13902–13913 (2013). doi:10.1021/jp4048659

38. W.-J. Yin, T. Shi, Y. Yan, Unusual defect physics in $CH_3NH_3PbI_3$ perovskite solar cell absorber. *Appl. Phys. Lett.* **104**, 063903 (2014). doi:10.1063/1.4864778

39. S. Colella, E. Mosconi, P. Fedeli, A. Listorti, F. Gazza, F. Orlandi, P. Ferro, T. Besagni, A. Rizzo, G. Calestani, G. Gigli, F. De Angelis, R. Mosca, $MAPbI_{3-x}Cl_x$ mixed halide perovskite for hybrid solar cells: The role of chloride as dopant on the transport and structural properties. *Chem. Mater.* **25**, 4613–4618 (2013). doi:10.1021/cm402919x

40. G. Giorgi, J.-I. Fujisawa, H. Segawa, K. Yamashita, Cation role in structural and electronic properties of 3D organic-inorganic halide perovskites: A DFT analysis. *J. Phys. Chem. C* **118**, 12176–12183 (2014). doi:10.1021/jp504479c

41. A. Buin, P. Pietsch, J. Xu, O. Voznyy, A. H. Ip, R. Comin, E. H. Sargent, Materials processing routes to trap-free halide perovskites. *Nano Lett.* **14**, 6281–6286 (2014). doi:10.1021/nl502612m

42. X. M. Duan, C. Stampfl, Vacancies and interstitials in indium nitride: Vacancy clustering and molecular bondlike formation from first principles. *Phys. Rev. B* **79**, 174202 (2009). doi:10.1103/PhysRevB.79.174202

43. S. D. Stranks, V. M. Burlakov, T. Leijtens, J. M. Ball, A. Goriely, H. J. Snaith, Recombination kinetics in organic-inorganic perovskites: Excitons, free charge, and subgap states. *Phys. Rev. A* **2**, 034007 (2014). doi:10.1103/PhysRevApplied.2.034007

44. M. Razeghi, *Fundamentals of Solid State Engineering* (Springer, New York, ed. 3, 2009).